GRIDDING ARTIFACTS ON ENVISAT/MERIS TEMPORAL SERIES

Luis Gómez-Chova[1], Raul Zurita-Milla[2], Luis Alonso[1], Luis Guanter[3], Julia Amorós-López[1], Gustavo Camps-Valls[1], and Jose Moreno[1]

[1]*Image Processing Laboratory (IPL), University of Valencia, Spain*
[2]*Geo-information Processing Department, ITC, University of Twente, The Netherlands*
[3]*Institute for Space Sciences, Free University of Berlin, Germany*

ABSTRACT

Earth observation satellites are a valuable source of data that can be used to better understand the Earth system dynamics. However, analysis of satellite image time series requires an accurate spatial co-registration so that the multi-temporal pixel entities offer a true temporal view of the study area. This implies that all the observations must be mapped to a common system of grid cells (gridding). Two common grids can be defined as a reference: (1) a grid defined by an external dataset in a given coordinate system or (2) a grid defined by one of the images of the time series. The aim of this paper is to study the impact that gridding has on the quality of ENVISAT/MERIS image time series, which is quantified using a time series of images acquired over The Netherlands. First, the impact of the reference map grid selection is evaluated in terms of geolocation errors and pixel overlap. Then, the effect of observation geometry (due to the fact that images are acquired from slightly different orbits) is studied. Results show that it is of paramount importance to identify areas with small pixel overlap in order to further analyze the reliability of the products derived from these areas.

Key words: MERIS; satellite image; time series; gridding; resampling; mapping; pixel overlap.

1. INTRODUCTION

Obtaining reliable and up-to-date Earth's surface information is essential to better understand the Earth's system. In this respect, the MEdium Resolution Imaging Spectrometer (MERIS), on board the ENVISAT satellite, has a great potential for multi-temporal studies both at regional and global scales. MERIS temporal resolution allows delivering multispectral data at 300m over the globe with a revisit time of 2-3 days (Rast et al., 1999). Therefore, MERIS time series or, in general, time series from any medium resolution instrument, like MODIS (Salomonson et al., 1989), or the forthcoming OLCI on board GMES Sentinel-3 (Nieke et al., 2008), provides an excellent opportunity for monitoring Earth dynamics with convenient temporal and spatial resolution.

The analysis of MERIS time series poses, however, some challenges that, if unaddressed, can severely hamper the operational exploitation of these valuable data. For example, although the MERIS sensor has a large swath that allows a high revisit time, the ENVISAT platform only repeats orbit every 35 days. This means that most of the images of a given temporal series will be acquired from a (slightly) different orbit. This, in turn, implies that each of the MERIS images has a slightly different observation geometry. As a result, some differences in the instantaneous field of view of each pixel (pixel footprint) among the different dates are to be expected. These differences are also present even if only images acquired from the same orbit are selected (because of unavoidable small shifts in satellite position and in the image acquisition time). This geometric mismatch reduces the overlap between the pixel footprints of images acquired at different dates and can even result in a null overlap depending on the used mapping criterion. In these situations, the multi-temporal information to be extracted might present a much lower effective spatial resolution in the case of homogeneous areas; or might be completely wrong in the case of heterogeneous areas, since different land covers may be observed by each MERIS pixel.

This paper analyzes the methodologies that can be applied to co-register MERIS time series and the gridding artifacts that appear when assigning observations to a pre-defined system of grid cells. Basically, one can use (*i*) a predefined spatial dataset like an existing map of the study area (mapping to a uniform grid) or (*ii*) a given MERIS acquisition as a reference to co-register all the images of a time series. Once the multi-temporal pixel entities have been defined by one of these two approaches, one can analyze and quantify the trade-off between geolocation errors (distances) and spatial overlap (areas) between the actual pixels constituting each multi-temporal pixel entity (Julea et al., 2008). This will facilitate the elaboration of enhanced MERIS Level-3 products, which involve temporal and spatial composites, and will improve the usability of MERIS time series (Defourny et al., 2006; Vancutsem et al., 2007).

In the experiments, a MERIS time series acquired over The Netherlands is used to evaluate the impact of the gridding in the generation of colocated time series.

Proc. 'ESA Living Planet Symposium', Bergen, Norway
28 June – 2 July 2010 (ESA SP-686, December 2010)

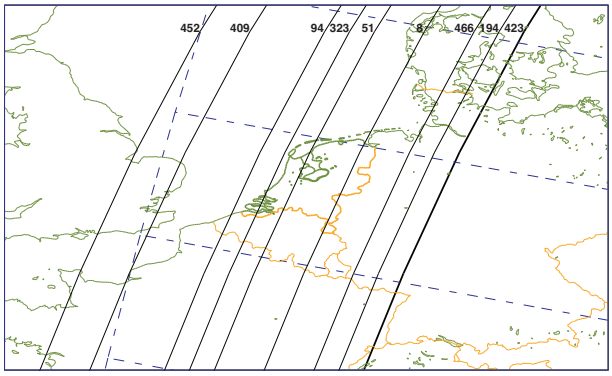

Figure 1. Orbit tracks of the selected images in the MERIS time series acquired over The Netherlands.

2. DATA MATERIAL

2.1. MERIS Level-1b Products

The MERIS data analyzed in this work consist of a time series of Full-Resolution (FR) images of *Geolocated and Radiometrically Calibrated Top of the Atmosphere Radiance* (L. Bourg and The MERIS Team, ACRI, 2006), i.e. the so-called MERIS FR Level-1b (L1b) product.

Push-broom sensors like MERIS have an array of detectors, placed transversally to the platform movement, that provides spatial sampling in the across-track direction, while the satellite's motion provides scanning in the along-track direction. Therefore, all measurements (pixels) in an image line are acquired simultaneously and correspond to a straight line on the Earth's surface if no instrumental errors (e.g. keystone or detector misalignment) occur. In the case of MERIS, the Earth is imaged with a spatial resolution of 260 m across-track and 290 m along-track at the nominal orbit, and the instrument's field of view (FOV) of 68.5° around nadir covers a swath width of 1150 km. As MERIS sensor elements have a nearly even angular spacing in the across-track direction, the distance between their projections on Earth surface increases towards the sides of the image lines (extreme look directions of MERIS swath), thus increasing the pixel footprint (integration area of the pixel), which will be larger in the across-track direction than the along-track direction (L. Bourg and The MERIS Team, ACRI, 2006). In general, the size of the sensor's footprint depends on the instantaneous field of view (IFOV), the distance from the platform to the target, and the observation angle with respect to nadir. However, in the MERIS L1b products delivered to the users, the original MERIS observations in Level-0 products are resampled to the Level-1b product pixels, which are regularly spaced along- and across-track. In this process, a nearest neighbor resampling is applied to fill the MERIS L1b product pixels with the original data. Thus, if the original observation covers two product pixels, the original radiances are copied to both product pixels and both are marked as *duplicate* in the MERIS quality flags.

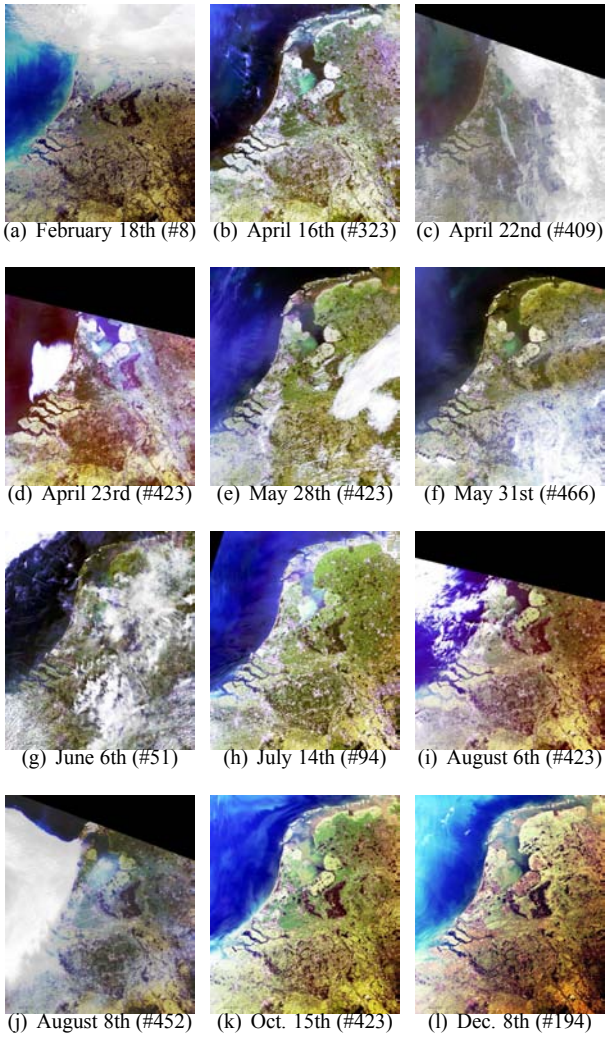

Figure 2. Co-registered MERIS FR Level-1b time series acquired over The Netherlands in 2003 (# orbit number).

2.2. MERIS full resolution time series over The Netherlands

A time series of MERIS FR L1b images acquired over The Netherlands in 2003 was selected to illustrate this work. The image acquisition dates were chosen according to two criteria: (*i*) to maximize the number of different orbits in the series; and (*ii*) to have, at least, four images acquired from the same orbit. Therefore, the inter- and intra-orbit differences can be analyzed, respectively.

The orbit tracks of the images that form the time series are depicted in Fig.1. The first thick solid line on the right side highlights orbit #423 and the dashed lines depict the corresponding MERIS swath, which completely encompasses the territory of The Netherlands. The orbit #423, and particularly the image acquired October 15th, is used as reference image in our experiments (c.f. section 4). In Fig.1, one can also appreciate that the selected time series includes the full range of orbits that cover The Netherlands.

Fig.2 shows the RGB color composites of the MERIS images for the different dates indicating the relative ENVISAT orbit number in parenthesis. In this figure, the MERIS FR images are projected into the Dutch national system (RD) at 300 m (1083×939 pixels). The images were automatically projected using the geolocation information provided in the corresponding MERIS products (L. Bourg and The MERIS Team, ACRI, 2006). A nearest neighbor resampling method was used in this step in order to preserve the MERIS spectral information. A visual inspection of the projected MERIS images did not show any major shift between them (besides the expected differences due to different acquisition orbits). This can be considered as a preliminary quality proof of the automatic projection of the images (Bourg and Etanchaud, 2007). Although a quantitative assessment of the geolocation accuracy might have been more appropriate (Bicheron et al., 2008), the aim of this work is to test the operational use of MERIS FR L1b time series.

3. METHODOLOGY

This section reviews the proposed geometrical measurements and explains the need for different mapping approaches of time series for different applications.

3.1. Mapping image pixels to the grid cells

The first stage in the processing of satellite image time series is the co-registration of all the images into a common grid, which usually implies two steps that are intimately related:

1. To define the location and extension of the regions (grid cells) where the temporal evolution should be analyzed.
2. To select the observations of each date contributing to each generated multi-temporal pixel entity.

The first step usually defines a regular map grid in a predefined coordinate system (e.g. Geographic Lat-Lon, UTM, or the Dutch RD coordinate systems) for georeferencing the resulting temporal composite. However, if one only wants to co-register the images in the time series without mapping them into a fixed grid of geodetic coordinates, it is possible to use the pixel center coordinates of a reference image in the time series to define the mapping for the rest of the images (i.e. one of the images of the time series acts as a reference image). In the second step, each observation is allocated to the grid cell encompassing the observation center. However, when two or more observations map into the same grid cell, one has to choose the observation to be assigned to the grid cell using a selection criteria (or combine all different observations of the same grid cell). Usually, the observation falling closest to the grid cell center is selected, which is

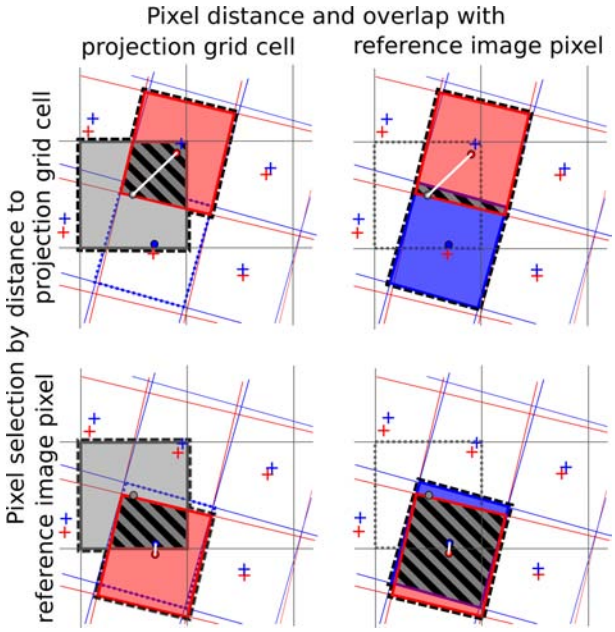

Figure 3. Representation of the four cases considered for measuring the resulting overlap and distance between pixels and grid cells: the reference frame is the map grid (left column) or a reference image (right column), and the selection of the image pixel is done by its distance to the center of the map grid cell (top row) or to the center of the reference image pixel (bottom row) to maximize matching between observations (pixel overlap). Boundaries are displayed for the map grid cells (grey grid), the analyzed image pixels (red grid), and the reference image pixels (blue grid). Pixel centers are marked with crosses. The selected image pixel is shown in solid red, the reference cell or pixel is in solid grey for the grid case and in solid blue for the reference image case. The polygons involved in the comparison are bounded by a black dashed line (union area). The overlap is striped with gray lines (intersection area) and a white straight line indicates the distance to the reference center.

equivalent to a nearest neighbor interpolation. This resampling method is commonly used in remote sensing applications since it leaves unaltered the signal measured by the sensor without artificially assuming any kind of spatial relation among neighboring pixels (e.g. linear or cubic) (Galbraith et al., 2003; Inglada et al., 2007). However, spurious effects may appear as a result of the repetition or omission of pixels (Cracknell, 1998). Moreover, this resampling method implies a spatial shift (geolocation error) between the observations and the assigned location that might hide a low correspondence (overlap) between pixels of different dates. It is worth noting that one might use an alternative gridding approach to maximize the overlap between the pixel footprints instead of minimizing the distance between image pixel and grid cell centers, but none of the standard gridding approaches consider the degree of overlap of observations (Tan et al., 2006).

Fig.3 illustrates how the measurement of pixel overlap and the geolocation errors[1] strongly depend on (*i*) the criteria used to select the pixel to be analyzed (rows), and (*ii*) the reference frame used to make the comparison (columns). The pixel selection can be done by minimizing its distance to the center of the map grid cell (top row) in order to minimize geolocation errors, or to the center of the reference image pixel (bottom row) in order to maximize the matching between observations (pixel overlap). Additionally, one also has to consider that the overlap and the geolocation errors of the image pixels can be computed with respect to the map grid (left column) or the reference image (right column). These two geometric measurements are used to provide some insights into the quality of each generated multi-temporal pixel entity. For instance, the upper-right plot in Fig.3 illustrates how, if the series of images is projected into a predefined map grid minimizing the distance to the grid cell centers, some pixels might have very little overlap with the pixels of other images (in this case the image used as a reference).

3.2. Time series quality indicators

In order to quantify the gridding effects on satellite image time series, one can compute the matching of image pixels from each date with both the map grid cells and the reference image pixels. In this work, the root mean square (RMS) absolute geolocation error (*distance*) and the pixel overlap (*area*) are used to quantify the matching. These quality indicators are computed between each pixel of a given image (t) and both the assigned grid cell (g) and the associated pixel from the reference image (r). In addition, they are computed for both pixel selection approaches (depending on if the selection of the pixel is done attending to a reference image or to the map grid) as presented in Fig.3.

Given an image pixel i at an acquisition time t, let us define its center coordinates as $\mathbf{x}_i^{(t)}$, and its corresponding footprint (modeled as a polygon that characterizes the geographical area observed at this time) as $\mathbf{P}_i^{(t)}$. Then, one can define two complementary quality metrics:

- The RMS geolocation error is computed as the distance (lat-lon coordinates) between the centers of the pixel of the analyzed image and the associated map grid cell:

$$d_i^{(g)} = \|\mathbf{x}_i^{(t)} - \mathbf{x}_i^{(g)}\|^2. \quad (1)$$

  Analogously, the distance with the associated pixel from the reference image is computed as $d_i^{(r)} = \|\mathbf{x}_i^{(t)} - \mathbf{x}_i^{(r)}\|^2$.

- The relative pixel overlap is computed as the ratio of the intersection area over the union area of the polygons defined for the image pixel and the map grid cell (or with the pixel of the reference image: $o_i^{(r)}$):

$$o_i^{(g)} = \frac{area(\mathbf{P}_i^{(t)} \cap \mathbf{P}_i^{(g)})}{area(\mathbf{P}_i^{(t)} \cup \mathbf{P}_i^{(g)})}, \quad (2)$$

  where operators $\cap$ and $\cup$ represent the intersection and union of polygons, respectively.

It must be noted that the overlap in Equation 2 is relative to the common area (union area) so it ranges from zero (no overlap) to one (equal polygons) and thus it can be expressed in percentage (e.g. an overlap of 30% represents the case of two equal-size pixels with their centers separated by a half-pixel). A different overlap measure is described in Wolfe et al. (1998), which divides the intersection area between the observation and the grid cell by the area of the observation, but Equation 2 is used in this work since it can also compare pixel footprints of different sizes. In this work, the overlap has been obtained by first projecting an image with the index number of all pixels into a fix grid with a much higher spatial resolution (HR) than the nominal resolution of the satellite sensor (25 m and 300 m, respectively), and then computing the overlap by counting the common cells on the HR grid. Note that, with this procedure, the accuracy of the computed overlap depends on the number of pixels of the HR grid that conform a cell, but using a HR-grid cell size 12 times smaller than the low resolution pixel size, the introduced errors are negligible.

4. EXPERIMENTAL RESULTS

4.1. Impact of the gridding pixel selection criteria

This section focuses on the implications of the pixel selection approach used. That is, whether an image pixel assigned to a given location (grid cell) is selected attending to the distance between its center and the map grid cell or to the nearest pixel of the reference image. Results for the image acquired on May 31st (orbit #466) are shown in Fig.4. As mentioned in section 2.2, the image acquired on October 15th (orbit #423) is used as reference for the temporal composition, and the map grid consists of 300×300 m cells in the Dutch RD coordinate system.

The differences between pixel footprints for the two images are due to the different acquisition orbits for the two dates (#466 and #423) and they vary across the image producing a Moiré pattern[2] easily observed in Fig.4. These plots show the pixel overlap patterns for a 100×100 cells window in the Dutch RD coordinate system of a region in the center of The Netherlands.

The overlap between the selected image pixel and the grid cell $o_i^{(g)}$ is shown in Fig.4(a&b), whereas the overlap between the selected image pixel and the reference image

[1] Geolocation error is defined in this work as the distance between the center of the original MERIS pixel product and the center of the grid cell to which this pixel is assigned.

[2] A Moiré pattern is the interference pattern obtained when two grids are overlaid at an angle or when they have slightly different mesh sizes.

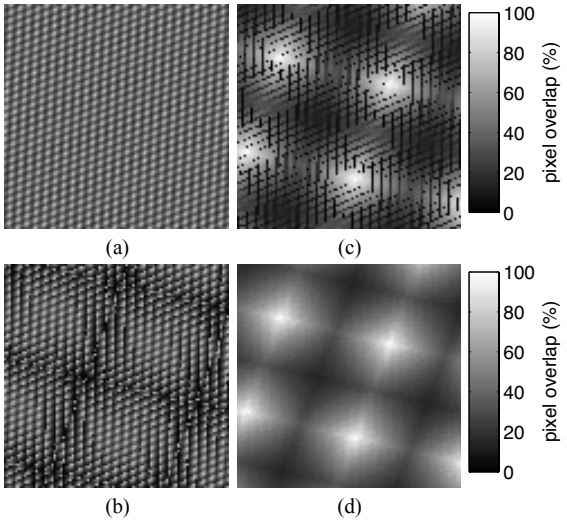

Figure 4. Pixel overlap for different pixel selection approaches and reference grids. The plots show results in a 100×100 *cells window: Overlap with grid cells (a) and with reference image pixels (c) when selecting pixels by their distance to grid cells; Overlap with grid (b) and with reference image pixels (d) when selecting pixels by their distance to reference image pixels. Note the correspondence between these plots and the plots in Fig.3.*

pixel $o_i^{(r)}$ is shown in Fig.4(c&d). Note that two subplots are needed for each case because of the different criterion to select the pixels. Thus, the subplots (a&c) illustrate the pixel selection based on minimizing the distance to the grid cell, and the subplots (b&d) illustrate the selection based on minimizing the distance to the reference image pixels.

Results obtained when image pixels are selected by their distance to the grid cells are analyzed first, since this is the most common approach in multi-temporal remote sensing applications. In Fig.4(a), one can appreciate a fairly homogeneous distribution of pixel overlap with the grid cells that can be explained since the image pixels assigned to each grid cell have been selected by minimizing its distance to the grid cell $d_i^{(g)}$, which in turn maximizes the overlap $o_i^{(g)}$ between them. However, with this approach, pixels of different dates are selected attending only to their relation to the grid without imposing any relation between the pixels that will form the multi-temporal pixel entity. This can be seen in Fig.4(c) where, in some grid cells, the overlap between the analyzed and the reference image pixels drops off drastically and even would produce temporal composites with no spatial overlap in some elements. Obviously, this situation is unacceptable for the analysis of time series except over extremely homogeneous regions where a spatial shift will not deviate the combined radiometric information from the ideal case.

The other option is to select the image pixels by their distance to the pixel centers of a reference image of the time series. In Fig.4(d), the distribution of pixel overlap with

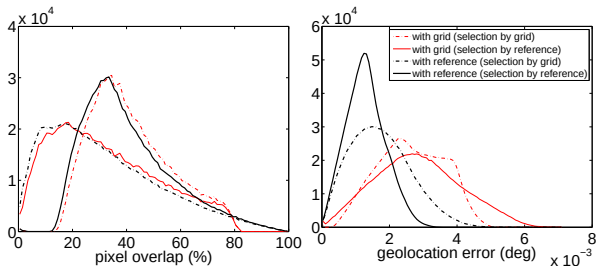

Figure 5. Histograms of pixel overlap and geolocation error between the pixels of the analyzed image and the grid cells (red lines) or the reference image pixels (black lines) selecting the pixels assigned to each cell by their distance to the grid cells (dashed lines) or to the reference image pixels (solid lines).

the reference image pixels shows the same Moiré pattern than before but, in this case, all cells present an overlap of, at least, 17%. Therefore, by selecting the image pixels assigned to each grid cell minimizing their distance to the reference image pixels $d_i^{(r)}$, the overlap between pixels $o_i^{(r)}$ is maximized and the extreme low overlap values visible in Fig.4(c) disappear in Fig.4(d). On the contrary, the overlap of the image pixels with the grid cells (Fig.4(b)) in those pixels that change is also reduced.

In order to better analyze the results, Fig.5 shows the histograms of the pixel overlap and the geolocation error for all the cases but taking into account the whole region over The Netherlands (1083×939 cells). In these plots, one can better analyze the distribution of values and their limits. First, one can observe the complementary behavior of the overlap between the pixels of the analyzed image and the grid cells (red lines) or the reference image pixels (black lines) depending on the used selection criterion (dashed and solid lines). Basically, with regard to overlap, results show that independently of the selection approach an overlap with the map grid cells is never higher than 80%. Overlap with the reference image occasionally reaches 100%, however, the greatest number of cases fall below 50%. It is important to note that whenever the selection and the overlap use different criteria, the pixel overlap goes down to zero with the maximum of the histogram about 20%. On the other hand, regarding geolocation errors, the distance to a reference image is always smaller than the distance to a grid. Thus, it can be concluded that for multi-temporal analysis it is better to use a reference image to select the appropriate pixels to construct the multi-temporal pixel entity, as the distance between centers is minimized throughout the image, while the overlap is maximized reaching cases with almost 100% overlap.

Summarizing, pixel selection criteria has a great impact on the results, so the choice of a pixel selection approach depends on the requirements of the application. An application demanding a high geolocation accuracy of the results retrieved from the generated time series (e.g. urban growth, floods, deforestation, fire damage, sub-pixel classification, inland water monitoring, etc.) should se-

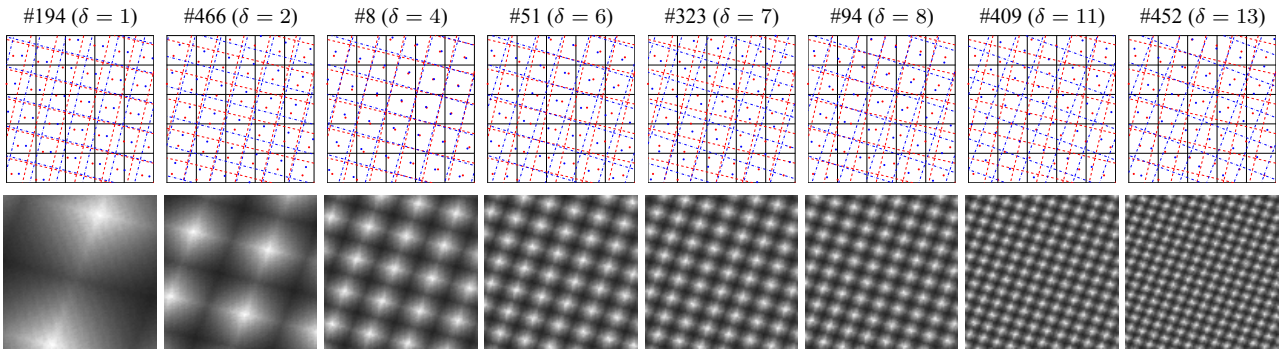

Figure 6. Results for images with an orbit different from that of the reference image (October 15th, orbit #423) sorted by the longitudinal distance between the orbit of the reference image and the orbit of the analyzed image (number of orbit shifts δ in parenthesis). First row*: map grid (*5×5 *cells) overlaid with pixel footprints of the reference image (blue) and the analyzed image (red).* Second row*: Overlap with reference image pixels when selecting pixels by their distance to reference image pixels (*100×100 *cells).*

lect the image pixels assigned to the grid cells by minimizing their distance to the grid cells $d_i^{(g)}$. However, in this case, the user should be aware of the grid cells where the overlap is extremely low, since in these locations the retrieved biophysical products may be less accurate or even wrong. Therefore, in multi-temporal applications, the overlap image shown in Fig.4(c) should be computed and used as a quality indicator (e.g. quality flags can be obtained to identify all pixels under a given overlap threshold). Analogous conclusions are obtained when the image pixels assigned to the grid cells are selected by minimizing their distance to the reference image pixels $d_i^{(r)}$. This approach is more suitable for applications where the consistency of the temporal information in a given area is critical (e.g. crop phenology, vegetation dynamics, desertification, urban monitoring, etc.). Furthermore, the overlap information contained in Fig.4(d) is also relevant to know in which areas the retrieved products are more consistent (higher overlap) and Fig.4(b) allows identifying cells where the provided information does not correspond to the map location accurately.

4.2. Impact of the orbit selection on satellite image time series

Once the effects of the pixel selection criterion and the resampling have been analyzed, this section explores their dependence on the orbit difference between images for the full time series. In order to properly interpret the results, one should recall Fig.1 and observe that orbits of the satellite image time series are distanced from the reference orbit (#423) westward at constant increments (although the time series does not comprise all possible orbits in this range and some gaps can be observed). This longitudinal increment in the west direction from the reference orbit (hereinto referred to as *orbit shift*, δ) is used to sort the image results in Fig.6 since it expresses the difference between the orbits and the observation geometries. Therefore, orbit order from left to right corresponds

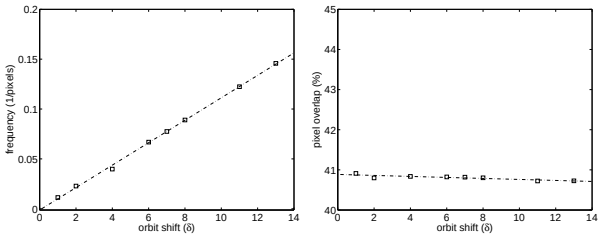

Figure 7. Spatial frequency, and average value of the overlap patterns as a function of the orbit shift (δ) with respect to the reference orbit.

to an increase in the distance in the west direction with respect to the reference orbit. Pixel overlap in the second row of Fig.6 shows the expected Moiré patterns where the orientation of the patterns depends on the orbit inclination, which determines the orientation of the sensor scanning. Moreover, the spatial frequency of the patterns increases as the longitudinal distance between orbits increases, which produces an increasing angular shift between the pixel footprint gratings of the images, as can be seen in the first row of Fig.6. Despite the apparent differences between the overlap spatial patterns depending on the orbits, the overlap histograms show almost identical curves to the ones presented in Fig.5: the pixel overlap ranges from 0% up to 80% when the selection of the image pixel is done by its distance to the center of the map grid (average overlap around 32%), and from 17% up to almost 100% when it is done by its distance to the center of the reference pixel (average overlap around 41%). These results are valid for images acquired at The Netherlands latitudes, but similar behavior is expected at other latitudes.

Fig.7 shows the properties of the overlap patterns of the whole scene in the Fourier spectral domain to further analyze the differences in the pixel overlap patterns as a function of the orbit shift (δ). It shows the spatial frequency (fundamental frequency of the two-dimensional Fourier transform) of the overlap patterns. The spatial frequency of the patterns presents a linear dependence with the orbit

shift (δ), which can be explained since the variation in δ produces a linear variation in the angle between the pixel gratings of the images. Moreover, the average pixel overlap for all the orbits is 41% approximately, which demonstrate that the produced overlap patterns present different spatial distributions but the same distribution in values (only the spatial frequency changes).

In the case of images acquired from the same orbit, one would expect that the average pixel overlap should be much higher since they present almost the same observation geometry. However, and very importantly, when there are small shifts in the satellite position or geolocation uncertainties (across-track direction) or shifts in the starting acquisition time (along-track direction), the pixel grating for both images is the same but with a constant spatial shift. Therefore, the mismatch between pixels from the two dates is the same for all the image pixels and, depending on the shifts, the relative pixel overlap for the whole image might be lower than 20% (being these images useless for temporal studies). Top plots of Fig.8 show a subset of the map grid (5×5 cells) overlaid with pixel footprints of the reference image of October 15th and the images of April 23rd, May 28th, and August 6th acquired from the same relative orbit (#423). These examples illustrate three different scenarios that clearly affect the resulting pixel overlap displayed in the bottom plots of Fig.8. In the first case (April 23rd), the two pixel gratings are accurately colocated (small shift in the across-track direction can be observed) and the average pixel overlap for the whole image is 60%. In the second case (August 6th), the shift between the grids in the across-track direction is approximately half pixel (worst case in the across-track direction) and the overlap decreases to 37%. Finally, the third case (May 28th) present a small shift in the across-track direction and a shift of half pixel in the along-track direction (due to differences in the starting acquisition time) that drastically drop off the overlap to 25%, which is close to the worst-case scenario.

Attending to the previous results, for both selection approaches and independently of the image orbits, it is of paramount importance to identify the areas with rather small overlaps in order to analyze the validity of further multi-temporal studies in these areas and dates (e.g. biophysical parameter estimation). Moreover, one cannot assume that the matching between images acquired from the same orbit is perfect. Therefore, possible spatial shifts between image pixels should be taken into account to discard from the time series those images with low average overlap.

5. CONCLUSIONS AND DISCUSSION

The impact of gridding artifacts on MERIS image time series has been analyzed in this work. The proposed methodology incorporates the geometric matching between the pixel footprints (overlap) in order to decide whether it is better to co-register the images to a predefined coordinate system or to a given acquisition used as a reference. Moreover, differences in the observed areas have been quantified in terms of geolocation errors (distances) and spatial overlap (areas) between the actual pixels constituting each multi-temporal pixel entity. This information may be used to elaborate enhanced products and to improve the usability of satellite image time series coming from the same or different orbits.

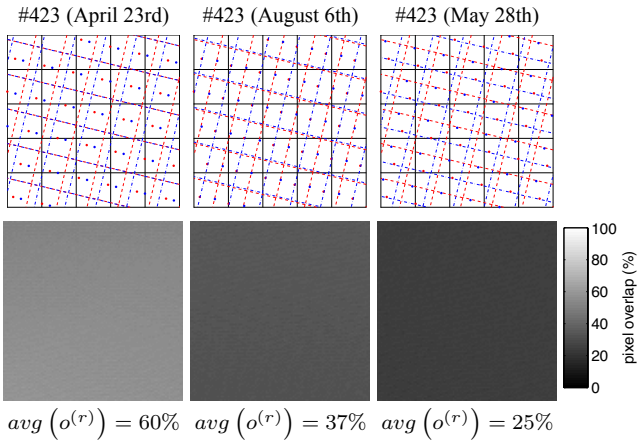

Figure 8. Results for images with same orbit as the reference image (#423, October15th, $\delta = 0$). Top row*: map grid (5×5 cells) overlaid with pixel footprints of the reference image and the analyzed image.* Bottom row*: Overlap with reference image pixels when selecting pixels by their distance to reference image pixels (100×100 cells).*

All these analyses are supported by a set of experiments carried out using a time series of MERIS FR L1b images acquired over The Netherlands in 2003. Results have shown that the average pixel overlap between images acquired from different orbits is around 32% when the selection of the image pixel is done by its distance to the center of the map grid, and around 41% when it is done by its distance to the center of the reference pixel. Therefore, in both cases, it is very important to identify the areas with rather small overlaps in order to analyze the reliability of further estimated biophysical parameters in these areas. On the other hand, in the case of images acquired from the same orbit, the average pixel overlap can be much higher. However, under certain conditions (e.g. subpixel shifts), it might be lower than 20% being this image pair useless for temporal studies.

Further work is needed to explore accurate mapping approaches in order to obtain more realistic and accurate pixel footprint characterization. For example, in current MERIS L1b products, a regular sampling in the along-track and across-track directions is imposed in the products provided to the users with the corresponding loss of information for further geometric processing. However, when two resampled product pixels come from the same MERIS observation, both are marked as *duplicate*. This flag only allows a partial reversibility of the image-to-product resampling process and thus a more accurate vectorial model of the actual MERIS observed pixels might be obtained.

ACKNOWLEDGMENTS

This paper has been supported in part by the Spanish Ministry for Education and Science under projects EODIX/AYA2008-05965-C04-03 and CONSOLIDER/CSD2007-00018.

REFERENCES

Bicheron, P., Amberg, V., Bourg, L., Miras, B., Brockmann, C., Delwart, S., Goryl, P., Ranéra, F., Hagolle, O., and Arino, O. (2008). Geo-location assessment of MERIS Globcover ortho-rectified products. In Lacoste, H. and Ouwehand, L., editors, *Proceedings of the 2nd MERIS/(A)ATSR Workshop*, pages CD–Rom, Frascati, Italy. ESA SP-666, ESA Publications Division. 22-26 September 2008.

Bourg, L. and Etanchaud, F. (2007). The AMORGOS MERIS CFI (Accurate MERIS Ortho-Rectified Geolocation Operational Software) Software User Manual & Interface Control Document. Technical Report 3.0, ACRI-ST.

Cracknell, A. P. (1998). Review article. Synergy in remote sensing–what's in a pixel? *International Journal of Remote Sensing*, 19(11):2025–2047.

Defourny, P., Vancutsem, C., Bicheron, P., Brockmann, C., Nino, F., Schouten, L., and Leroy, M. (2006). GLOBCOVER: a 300 m global land cover product for 2005 using ENVISAT MERIS time series. In *Proceeding ISPRS Commission VII Mid-term Symposium "Remote Sensing: From Pixels to Processes", Enschede, the Netherlands, 8-11 May 2006*, pages 59–62.

Galbraith, A. E., Theiler, J. P., and Bender, S. C. (2003). Resampling methods for the MTI coregistration product. In Shen, S. S. and Lewis, P. E., editors, *Algorithms and Technologies for Multispectral, Hyperspectral, and Ultraspectral Imagery IX*, volume 5093, pages 283–293. SPIE.

Inglada, J., Muron, V., Pichard, D., and Feuvrier, T. (2007). Analysis of artifacts in subpixel remote sensing image registration. *IEEE Trans. on Geoscience and Remote Sensing*, 45(1):254–264.

Julea, A., Meger, N., Trouve, E., and Bolon, P. (2008). On extracting evolutions from satellite image time series. In *IEEE Int. Geoscience and Remote Sensing Symposium (IGARSS 2008).*, volume 5, pages 228–231.

L. Bourg and The MERIS Team, ACRI (2006). MERIS Level 1 Detailed Processing Model. Technical Report 7, European Space Agency.

Nieke, J., Frerick, J., Stroede, J., Mavrocordatos, C., and Berruti, B. (2008). Status of the optical payload and processor development of ESA's Sentinel 3 mission. In *IEEE Int. Geoscience and Remote Sensing Symposium (IGARSS 2008)*, volume 4, pages 427–430.

Rast, M., Bézy, J., and Bruzzi, S. (1999). The ESA Medium Resolution Imaging Spectrometer MERIS: a review of the instrument and its mission. *Int. Journal of Remote Sensing*, 20(9):1681–1702.

Salomonson, V., Barnes, W., Maymon, P., Montgomery, H., and Ostrow, H. (1989). MODIS: advanced facility instrument for studies of the Earth as a system. *IEEE Trans. on Geoscience and Remote Sensing*, 27(2):145–153.

Tan, B., Woodcock, C., Hu, J., Zhang, P., Ozdogan, M., Huang, D., Yang, W., Knyazikhin, Y., and Myneni, R. (2006). The impact of gridding artifacts on the local spatial properties of MODIS data: Implications for validation, compositing, and band-to-band registration across resolutions. *Remote Sensing of Environment*, 105(2):98–114.

Vancutsem, C., Bicheron, P., Cayrol, P., and Defourny, P. (2007). An assessment of three candidate compositing methods for global MERIS time series. *Canadian Journal of Remote Sensing*, 33(6):492–502.

Wolfe, R., Roy, D., and Vermote, E. (1998). MODIS land data storage, gridding, and compositing methodology: Level 2 grid. *IEEE Trans. on Geoscience and Remote Sensing*, 36(4):1324–1338.